Air Temperature Characteristics, Distribution and Impact on Modeled Ablation for the South Patagonia Icefield

C. Bravo[1], D. J. Quincey[1], A. N. Ross[2], A. Rivera[3,4], B. Brock[5], E. Miles[1], and A. Silva[3]

[1]School of Geography, University of Leeds, Leeds, United Kingdom.

[2]School of Earth and Environment, University of Leeds, Leeds, United Kingdom.

[3]Centro de Estudios Científicos, Valdivia, Chile.

[4]Departamento de Geografía, Universidad de Chile, Chile.

[5]Department of Geography and Environmental Sciences, Northumbria University, Newcastle upon Tyne, United Kingdom.

Corresponding author: Claudio Bravo (gycabl@leeds.ac.uk)

Key Points:

- Distinct lapse rates prevail on the east and west side of the icefield.
- A strong glacier cooling effect relative to off-glacier air temperature was observed.
- Ablation is estimated using temperature extrapolation approaches. Divergent results highlight the need for realistic temperature distributions.

Abstract

The glaciers of Patagonia are the largest in South America and are shrinking rapidly, raising concerns about their contribution to sea-level-rise in the face of ongoing climatic change. However, modelling studies forecasting future glacier recession are limited by the scarcity of measured on-glacier air temperatures, and thus tend to use spatially and temporally constant lapse rates. This study presents nine months of air-temperature observations. The network consists of five automatic weather stations (AWS) and three on-glacier air temperature sensors installed on the South Patagonia Icefield along a transect at 48° 45’ S. Observed lapse rates are, overall, steeper on the east (-0.0072 °C m^{-1}) compared to the west (-0.0055 °C m^{-1}) and vary between the lower section (tongue, ablation zone) and the upper section (plateau, accumulation zone) of the glaciers. Warmer off-glacier temperatures are found in the east compared to the west for similar elevations. However, on-glacier observations suggest that the glacier cooling effect is higher in the east compared to the west. Through application of distributed temperature-index and point-scale energy balance models we show that modelled ablation rates vary by up to 60%, depending on the air temperature extrapolation method applied, and that melt is overestimated and sublimation is underestimated if the glacier cooling effect is not included in the distributed air temperature data. These results can improve current and future modelling efforts of the energy and mass balance of the whole South Patagonia Icefield.

1 Introduction

On mid-latitude glaciers, near-surface air temperature is the main control on energy exchange over a snow or ice surface (Petersen et al., 2013, Shaw et al., 2016) and for glaciological applications, it is used as input for melt calculations ranging from empirical temperature-index (Hock, 2003) through to physically-based energy balance models (Greuell & Genthon, 2003). The air temperature is used to calculate the incoming longwave radiation and the sensible heat, and also where air temperature influences other variables such as moisture, which is used to calculate latent heat (Ebrahimi & Marshall, 2016). In terms of accumulation processes, the accurate distribution of air temperature over the glacier surface is essential for distinguishing areas where precipitation falls as rain or snow (Minder et al., 2010), and it also has a direct impact on snowpack metamorphism affecting snow redistribution (Carturan et al., 2015). Glacier mass balance models thus rely on accurate spatial distribution of the air temperature (Carturan et al., 2015).

Patagonia (40° S – 55° S) contains the largest glacierised area in South America, but recent evidence shows that most of these glaciers are shrinking rapidly (Foresta et al., 2018; Davies & Glasser, 2012; Malz et al., 2018; Meier et al., 2018; White & Copland, 2015). This deglaciation is primarily a matter of concern for sea level rise (Foresta et al., 2018; Gardner et al., 2013; Rignot et al., 2003, Willis et al., 2012). However, very little is known about how glacial areal changes and mass balance processes are linked to changes in climate (Malz et al., 2018; Pellicciotti et al., 2014; Weidemann et al., 2018). Overall, these changes are generally attributed to temperature increase as the glaciers in Patagonia are strongly sensitive to temperature change (Malz et al., 2018; Masiokas et al., 2008).This is because ablation is dominated by melt (Sagredo et al., 2012) . Thus, an in-depth understanding of air temperature variability and on-glacier near-surface meteorology is needed to understand the current and future state of these glaciers.

Previous research has described the steep gradients of some meteorological variables on the east side of the Southern Andes, which is a relatively dry 'rain shadow' leading to a foehn effect, while the windward west side experiences high precipitation and humidity and lower lapse rates (Lenaerts et al., 2014; Schneider et al., 2003; Smith & Evans, 2007). However, little attention has been given to the implications of these spatial contrasts for glacier mass balance and response to climate. Schneider et al. (2003) demonstrated a relationship between atmospheric circulation and glacier response, stating that wetter conditions caused by a change in circulation on one side lead to drier conditions on the other, and vice versa. Despite its importance for glaciological applications, there are no empirical studies of the spatial and temporal variability of air temperature over the surface of both sides of the Patagonian Icefields, and hence its significance to the climatic response of glaciers is unknown.

Vertical lapse rates, are the most common method of distributing air temperature in modelling studies (Marshall et al, 2007; Petersen & Pellicciotti, 2011; Wheler et al, 2014) and are one of the parameters to which melt models are most sensitive (Heynen et al., 2013). However, due to the complex boundary-layer meteorology of mountainous areas and the general lack of detailed on-glacier measurements (Hanna et al., 2017), constant and linear lapse rates are commonly used for glacier ablation estimations, rather than distributed air temperature fields for glacier ablation estimations (Ayala et al., 2015). This is a major simplification, as it has been widely recognized that air temperature lapse rates are spatially and temporally variable in mountainous regions (Petersen & Pellicciotti, 2011), both on-glacier (Ayala et al., 2015; Hanna et al., 2017; Shaw et al., 2017) and off-glacier (Heynen et al., 2016; Shen et al., 2016). Many studies use off-glacier data which do not account for the variability of the air temperature associated with katabatic boundary layer flows and the damping and ice surface cooling effect observed over glacier surfaces (Ayala et al., 2015; Carturan et al., 2015; Petersen and Pellicciotti, 2011; Petersen et al., 2013; Shaw et al., 2016). The cooling effect occurs under positive atmospheric temperatures as the lowest layers of air are cooled by sensible heat exchange with the underlying ice. The magnitude of the cooling effect is defined as the difference between screen-level temperatures over a glacier compared to equivalent-altitude ambient temperatures. This cooling is not homogenous over a glacier surface and depends on the geometric characteristics (Carturan et al., 2015). Cold dense air flows down glacier as a katabatic flow whose temperature structure can be simplified as a balance between adiabatic warming and cooling by sensible heat exchange with the glacier (Greuell and Böhm, 1998). Due to this reason, on-glacier lapse rates are typically lower than the environmental lapse rates (Shaw et al., 2017).

In Patagonia, a few reported lapse rates exist, but most are based on off-glacier observations. Regarding on-glacier observations, Takeuchi et al. (1996) and Stuefer et al. (2007) both estimated a lapse rate of -0.0080°C m^{-1} at the lower end of Perito Moreno glacier on the eastern side of the South Patagonia Icefield (SPI), while Popovin et al. (1999) reported an on glacier lapse rate for the small De Los Tres glacier, which is located outside the SPI. This study reported a mean lapse rate over the glacier surface of -0.015 °C m^{-1} over the terminus area, and noted frequent thermal inversions. Above 1,400 m a.s.l., the lapse rate reduced to -0.0017 °C m^{-1} (Popovin et al., 1999). While useful, these observations are limited by their short observation period of approximately 5 weeks, from 26 January to 4 March 1996.

Usually, mass balance modelling and temperature sensitivity analyses in Patagonia distribute the air temperature using the environmental lapse rate (ELR, -0.0060 to -0.0065 °C m^{-1}) (Barry, 2008) as a spatially and temporally constant value (Bravo et al., 2015; Kerr & Sugden, 1994; Schaefer et al., 2013; Schaefer et al., 2015). At best, studies use a monthly variable lapse rate (Mernild et al., 2016 following Liston & Elder, 2006), and distribute the air temperature using climate data from regional and global models. Constant lapse rates have also been used to extrapolate off-glacier meteorological data; for example, Rivera (2004) used a constant lapse rate of -0.0060 °C m^{-1} to distribute the monthly air temperature over Chico Glacier, and De Angelis (2014) used a constant lapse rate of -0.0080 °C m^{-1} to distribute daily air temperature across all the SPI.

Historically, meteorological observation on the plateau of the SPI has been difficult, due to the harsh weather conditions and the extreme logistical challenges. In spite of these restrictions, a weather station network was installed in 2015 (CECs-DGA, 2016), providing 9 months of continuous temperature measurements for a longitudinal profile at around 48° 45' S enabling spatial and temporal patterns of air temperature to be investigated.

In this work, we present an analysis of the air temperature and the lapse rates observed in this first Automatic Weather Station (AWS) network across the SPI. First, we describe the air temperature observations, concentrating on the spatial differences along the profile. Then, the vertical structure of the air temperature is analyzed at the glacier scale, and comparison between on-glacier and off-glaciers air temperature conditions are conducted. Finally, the impacts on ablation processes are assessed, for which we use both a distributed degree-day model and a point-based energy balance model to quantify the effects of different air temperature parametrizations on the modelled melt.

2 Materials and Methods

2.1 Study area and observations

The largest ice mass in Patagonia is the SPI which extends over 350 km between the latitudes 48°20'S and 51°30'S, along the meridian 73°30'W, with an area of ~13000 km^2 (De Angelis, 2014). The SPI comprises 48 main glacier basins, which end primarily in fjords on the western side and in lakes on the eastern side (Aniya et al., 1996). These glaciers are joined in the accumulation zone ("plateau"), with an average altitude of ~1,500 m a.s.l. The SPI is the second largest freshwater reservoir in the Southern Hemisphere, after Antarctica (Warren and Sudgen, 1993).

In recent decades, the majority of the outlet glaciers in the SPI have been retreating (Davies et al., 2012). Overall, White and Copland (2015) report a total area loss of 542 km^2 (~4% of the SPI) between the end of the 1970's and 2008-2010. Nevertheless, the rates and trends are neither homogeneous nor synchronous (Sakakibara & Sugiyama, 2014) and include episodes of advance (e.g. Pio XI glacier, Wilson et al., 2016).

This work focuses on the northern sector of the SPI (Figure 1) using data from a series of five AWSs, installed on proglacial zones and nunataks, running west-east across the ice divide. We take the AWS installed on the west side to be representative of glaciers Tempano (334 km^2), Occidental (235 km^2), Greve (428 km^2), HPS8 (35 km^2) and one unnamed glacier (41 km^2). AWSs installed on the east side are representative of glaciers O'Higgins (762 km^2), Pirámide (27 km^2) and Chico (239 km^2) (Figure 1) (DeAngelis, 2014).

Each AWS recorded a full set of meteorological variables between October 2015 and June 2016, comprising air temperature, relative humidity, wind speed and direction, incoming shortwave and longwave radiation and atmospheric pressure (Table 1). In addition, three ultrasonic depth gauges (UDGs) were installed directly on the glacier surface over the plateau. In the same structure, two air temperature sensors were also installed at an initial height of 2 and 4 m above ground level (a.g.l.). We call these Glacier Boundary Layer (GBL) air temperature stations (GBL1, GBL2 and GBL3 in Figure 1 and Table 1). We use these data to validate air temperature estimated with the different methods and to compare the ablation estimations. Unfortunately, the observations during three months (July, August and September 2016) are not complete or are completely absent, probably due the harsh weather conditions and logistical difficulties in recovering the data, hence we discard these periods.

The environment at proglacial and nunatak sites is influenced by local warming from solar heated rocks, although a partial influence of the glacier-boundary layer at these locations is expected. Two AWS (GO and GT) are proglacial stations. GT is located in a valley at a distance of 2.5 km from one of the calving fronts of the Tempano glacier, separated from the glacier by a fjord and by a hill of ~350 m a.s.l. At the time of the measurements, GO was located approximately 0.5 km from the glacier terminus, separated from the ice by a small branch of the O'Higgins lake. Three AWS (HSNO, HSG, HSO) are located on nunataks on the plateau. HSNO is located on a small nunatak (1.8 km^2 in area) on the Greve glacier. This AWS is located 100-150 m above the elevation of the tongue of the glacier but a sector of the nunatak, east of the AWS, is still covered by ice. HSG is located on a narrow nunatak (1.6 km^2 in area). The relative height over the plateau of the location of HSG reaches 50-60 m of the west side of the nunatak and 10-15 m to the east side of the nunatak. HSO is also located on a nunatak (2.8 km^2 in area) close to the elevation of the Equilibrium Line Altitude (ELA) of the O'Higgins glacier. This AWS is located at a relative height over the glacier surface of 50 to 250 m.

Air temperature sensors were installed in a naturally ventilated radiation screen. Errors due to radiative heating of the sensors are likely to be minor due to the prevalence of strong winds over the icefield (Garreaud et al., 2013). Except for HSG all the stations have 100% of the observations during the periods indicated in Table 1. A gap of data was detected in HSG, between the hours 2100 and 2200, for the entire observation period. These gaps were filled using linear interpolation. We take the measurements error to be that declared by the manufacturer (Table 1) and unfortunately, no inter-comparison was possible as the AWS and GBL were installed at different dates. The air temperature sensors at 4 m were used to verify the observations at 2 m.

2.2 Lapse rates

We concentrate our analysis on the observed lapse rates (LRs) between AWSs, and their spatial and temporal differences. For calculation of LRs, it has been suggested that multiple measurements should be used, as this allows calculation of the strength of the relationship between air temperature and elevation (Heynen et al., 2016). We thus calculate the SPI LRs from the regression of all mean temperature values, and the measure of the strength of the elevation dependence is provided by the determination coefficients (R^2) of the linear regression. In addition, to establish the differences between the western and eastern sides of the Icefield, stepwise air temperature lapse rates were estimated at hourly intervals.

As HSG is located 2.9 km from the glacier divide (Figure 1), the LRs for the west side were estimated between GT-HSNO and HSNO-HSG and on the east side between GO-HSO and HSO-

HSG. The observed air temperatures at GBL1, GBL2 and GBL3 were used to assess how representative the different extrapolation methods are of temperatures within the glacier surface layer.

2.3 Air temperature distribution

Based on these observations we apply five different extrapolation methods to simulate air temperature distribution, using air temperatures observed in HSNO for the west side and HSO for the east side as the primary input datasets. For all five methods, the hourly air temperature was distributed using the LP DAAC NASA Version 3 Shuttle Radar Topography Mission Digital Elevation Model (hereafter, SRTM DEM; NASA JPL, 2013) using the local UTM zone 18S. Considering the hypsometry of this zone and to maximize computational efficiency we resampled the SRTM DEM to 200 m resolution.

First, air temperature was distributed using a constant LR of -0.0065 °C m^{-1} (Barry, 2008) corresponding to the ELR. This value is the most commonly used value in the literature for glaciological and hydrological modelling (e.g. Schaefer et al., 2015).

Second, the seasonal mean observed LRs (MLR) were used to characterize the spatial differences between east and west sides and also between the plateau and the tongue of the glaciers.

Third, stepwise observed and hourly variable LRs (VLR) were applied. This method includes both spatial and temporal variability. On the west side, we used the GT-HSNO lapse rate between 0 and 1,040 m a.s.l. and the HSNO-HSG lapse rate between 1041 and 3,500 m a.s.l. (the highest point). On the east side, we used the GO-HSO lapse rate between 250 m (approximately the elevation of the front of O'Higgins glacier) and 1234 m a.s.l. and the HSO-HSG lapse rate between 1,235 and 3,500 m a.s.l.

As the second and third methods use data from both proglacial and nunatak weather stations, they represent non-glacial surface temperatures rather than the glacier-boundary layer temperature. Hence VLR corresponds to the variable atmospheric lapse rate. For input to a glacier ablation model the air temperature using VLR must be adjusted for the glacier boundary layer cooling effect. The fourth method therefore compared the VLR air temperatures with observations from on-glacier sensors (VLRBias). GBL2 is assumed to be representative of the west side and GBL3 of the east side. The adjustment of the air temperature (T_{vlra}) consists of a bias-correction of the data using the following expression (Teutschbein & Seibert, 2012):

$$T_{vlra} = T_{vlr} + \mu_m(T_{obs}) - \mu_m(T_{vlr}) \quad (1)$$

where T_{vlr} is the air temperature estimated with the VLR method at the elevation of the GBL2 on the west side and of the GBL3 on the east side, and μ_m is the mean of the observed air temperature at GBL2 and GBL3 (T_{obs}) and of the T_{vlr}. This approach is the same as that adopted by Ragettli et al (2013) and Ayala et al. (2016) for glaciers in Central Chile. Considering that the time series of GBL2 and GBL3 are shorter (Table 1), it is assumed that the difference in the mean is constant along the period and is isotropic. This approach attempts to replicate data observed on-glacier rather than AWSs off-glacier alone. We only used data from GBL2 and GBL3, considering that the air temperature sensor in GBL1 was installed at 1.2 m.

Finally, the fifth method corresponds to the method of Shea and Moore (2010; SM10 hereafter) which was then applied to alpine glaciers by Carturan et al. (2015) and Shaw et al. (2017). The advantage of this method is that it uses off-glacier data to extrapolate the air temperature and is a function of the flowline distance which is the average from a summit or ridge (Shaw et al., 2017). In our case, the distance was calculated using the SRTM DEM (Figure S1). The air temperature is estimated using a statistical model that accounts for the differences between ambient temperature and on-glacier temperature:

$$T_{sm10} = \begin{cases} T_1 + k_2\,(T_{vlr} - T^*), & T_{vlr} \geq T^* \\ T_1 - k_1\,(T^* - T_{vlr}), & T_{vlr} < T^* \end{cases} \quad (2)$$

T_{vlr} is representative of the free atmospheric air temperature. k_1 and $k_2$are parameters obtained from the slope of the linear piecewise regression, modeled as exponential functions of the flow distance. These parameters related the 2 m air temperature with the free atmospheric temperature (Figure S1) below and above the threshold T^*which is defined as a function of the flow distance (D_f) (Carturan et al., 2015; Shaw et al. 2017):

$$T^* = \frac{C_1\ D_f}{C_2 + D_f} \quad (3)$$

where $C_1$and $C_2$are 6.61 and 436.04 respectively; corresponding to fitted coefficients. $T_1$is the air temperature threshold for katabatic effects and is calculated as $T^* \cdot k_1$.

The parameters used in this model are the same as those used by Shea and Moore (2010) as the three on-glacier observation sites in this study are insufficient to define a new exponential curve. However, the resulting factors ($k_1$and k_2) obtained are compared with those used by Shea and Moore (2010) and Shaw et al. (2017). In the case of GBL1 and GBL2 the factors agree with the previous curves of $k_1$and k_2, but, the GBL3 factors do not (Figure S1). Considering the distance of GBL3 to the nearest ridge is expected that the factors, $k_1$and k_2, reach values close to 1, however, we obtained values around ~0.5 (Figure S1).

2.4 Melt and ablation models

Two models commonly used in the glaciological literature were applied to quantify the impact of air temperature distribution method on the melt and ablation over the SPI surface. First, a standard degree-day model (DDM) (e.g. Hock, 2003, 2005) was used with an hourly time step for each air temperature distribution. We chose this model over an Enhanced Temperature Index model (Pellicciotti et al., 2005), as the purpose is to identify the impacts of the air temperatures in the model, rather than quantify the real melt of these glaciers. This basic model has been used to predict future response of glaciers worldwide in many recent works (e.g. Bliss et al., 2014; Davies et al., 2014; Radic et al., 2014) and so, it is important to evaluate the corresponding parameters and assumptions used. In this model, the melt is assumed to increase linearly with air temperature above a given critical threshold assumed in this case to be at 0°C. The only data requirement is air temperature and empirically calibrated degree-day factors (DDF) that are used to scale the air temperatures to melt rates (Tsai and Ruan, 2018). The DDFs account for the different properties of snow, firn and ice (Mackay et al., 2017). As we do not have enough data to calibrate the DDFs, as for example stake measurements in the east side, we used a range of values between 3 mm w.e. $°C^{-1}$ d^{-1} and 10 mm w.e. $°C^{-1}$ d^{-1} based onprevious work (Hock, 2003; 2005).

The second model is an energy balance at the point-scale where meteorological observations are available. Radiative fluxes (incoming shortwave and longwave radiation) and the meteorological inputs (wind speed, relative humidity and atmospheric pressure) were taken from HSNO (west) and HSO (east) observations. Air temperature input is also variable depending on the method used for air distribution. As the air temperature distributions of the ELR, MLR and VLR were extrapolated from the observations at HSNO and HSO, at this elevation the observed air temperature is the same as that obtained from these methods. Hence, energy balance was calculated using VLR, the VLRBias and the SM10 air temperatures. Energy available for melt (W m^{-2}) was determined following Oerlemans (2010), assuming that the conductive heat flux and sensible heat brought to the surface by rain or snow are considered negligible. Indeed, recent work calculated 1 Wm^{-2} for sensible flux due to rain and 4 W m^{-2} for ground heat flux (Weidemman et al., 2018) for two glaciers in the south of our study area. Surface temperature is assumed constant at 273.15 K (0 ◦C). The heat fluxes were calculated using the bulk approach (Cuffey and Paterson, 2010) and stability corrections were applied to turbulent fluxes using the bulk Richardson number, which is used to describe the stability of the surface layer (Oke, 1987).

The complete set of equations used for the calculations of the turbulent fluxes are presented in Bravo et al. (2017) and references therein.

4 Results

4.1 Characterization of the observed air temperature

The observed 2 m daily and hourly mean of the air temperature for each station are shown in Figure 2. Lower air temperatures are recorded at the higher elevation AWS (HSG) and positive daily means at this high elevation site (1,428 m a.s.l.) are observed in summer months and even in fall where it is possible to see inversion episodes of the air temperature. Hence higher values are observed on the plateau when compared with off-glacier values.

The off-glacier air temperature shows positive values throughout the observational period with higher mean values generally registered at GO despite being located at a higher elevation than GT. At similar elevations, air temperatures at GBL1 are lower than at HSG, except in February. We associate this difference with the cooling effect of the glacier surface (Carturan et al., 2015), as HSG is installed on the rock surface and GBL1 is on snow on the glacier surface. The daily mean amplitude is higher on the west at GT (~4.5°C) compared with eastern AWS GO (~2°C).

The diurnal temperature range is higher at the off-glacier AWS compared to on-glacier AWS (Figure 2), revealing the dampening effect of the ice surface. The hourly mean values show that the highest Pearson's correlations coefficients (r) are between plateau air temperatures (Table S1) with r>0.88 in almost all the cases. The r between off-glacier temperatures and plateau temperatures are in all cases <0.52. The r between the AWS on the west side (GT and HSNO) is 0.44 and 0.47 between the eastern AWS (GO and HSO). The correlation is higher if the time series are compared between October and March with 0.67 and 0.59, respectively. Large-scale climate anomalies during the austral fall (Garreaud, 2018) lead to a lower correlation between off-glacier

AWS and on-glacier and nunataks AWS. The observations reveal that this circulation pattern increases the air temperature over the plateau more than over the off-glacier sites. Interestingly, r between both off-glacier (67 km distance) air temperatures is 0.77.

4.2 Lapse rates at glacier scale

The comparison between monthly mean air temperature and the elevation of the AWS on the SPI (Table 2) shows that LRs are highly linear with Coefficient of Determination (R^2) values over 0.90 from October to March. In the fall months this correlation diminishes to values close to 0.61 and during May the R^2 value is very low (0.18) when using all AWSs, suggesting an important control other than elevation at this scale (Figure S2). Spatially and temporally, the LRs estimated are steeper in the east compared to the west. Both sides show higher R^2 values (0.99) when considered separately, with the exception of fall (Table 2).

The stepwise hourly LRs show a range of values (Figure 3, Table 2). The estimated hourly observed lapse rate between each pair of AWS shows that on the west side, LRs are shallower (mean value -0.0055 °C m^{-1}) compared with the LRs observed on the east side (mean value -0.0072 °C m^{-1}). Mean values of LR on the west side (GT-HSNO and HSNO-HSG) are close to the ELR (-0.0065 °C m^{-1}). On the east side, the mean values are between the ELR and the dry adiabatic lapse rate (DALR, -0.0098 °C m^{-1}). On the east side, the plateau LRs (HSO-HSG) are steeper than the tongue LRs (HSO-GO). On-glacier lapse rates (GBL1 and GBL2) are shallower, with values in October, November and December close to -0.0040 °C m^{-1} followed by predominantly thermal inversions episodes in January and February (Figure S2).

In the west, GT-HSNO shows higher variability than the HSNO-HSG rate. In the latter case, the mean values and the median for each month are close to the ELR, while mean and median values for GT-HSNO show higher inter-monthly variability. In the east, the difference between GO-HSO and HSO-HSG is less evident. In both cases, during the spring and summer months, the LRs are between the ELR and the dry adiabatic lapse rate. LRs calculated for the HSO-HSG show a great number of steeper negative outlier values.

Thermal inversions are observed on both sides of the divide. Multi-site regression and stepwise statistics show that these episodes are more frequent on the west side, especially during fall. The data in Table 2 show that the episodes of thermal inversion are not necessarily concordant between the lower and the higher part of the glaciers on each side. Interestingly, the time series for the east side shows that a plateau (HSO-HSG) thermal inversion could occur with decreasing temperatures on the tongue (GO-HSO) and vice-versa. On the west side, it is also possible to identify episodes of thermal inversion on the tongue (GT-HSNO), meanwhile, the plateau (HSNO-HSG) shows a decrease in temperature with elevation. Therefore, a more complex structure in the air temperature lapse rates is detected. The lower R^2 values coincide with more frequent thermal inversion episodes, but, an important difference is that the signal of the thermal inversion in the fall months, especially May, is not strong in the distribution of the LRs of HSNO-HSG.

4.3 Air temperature distribution

A comparison of the observed air temperature (GBL) with air temperature extrapolated using the VLR method (Figure 4) shows an offset, especially at GBL1 (Figure 4a) and GBL2 (Figure 4b).

This offset is associated with the cooling effect that off-glacier and nunatak air temperatures observations cannot account for. The variability of the time series is almost the same, especially GBL1 and GBL2 where the correlation coefficients are 0.98 and 0.92, whereas in the location of GBL3 it is 0.54 (Figure 4c). Comparing these two time series reveals that spatial differences exist regarding the cooling effect. The observed on-glacier air temperature shows that the cooling effect on the west side reaches a mean value between 0.8°C (GBL1) and 1.3°C (GBL2) while on the east side it reaches 3.3°C, with significantly more scatter (GBL3, Figure 4c). The strength of the glacier cooling effect could be also related to humid conditions on both sides. Figure 4 shows that under lower relative humidity values, the differences between VLR and the observed air temperatures are higher, and hence the correlation is poor, especially at the GBL3 location (Figure 4c). We verified these data by comparing the observations from the same station at 4 m; the correlation coefficient is 0.95 and the mean difference is 0.6°C. As the differences become more pronounced with lower values of relative humidity, and the east side is drier than the west side, we might expect to see greater differences in the east.

The mean values of the air temperature distribution for each of the methods are presented in Figure 5. At comparable elevations, warmer conditions are observed in the east using the ELR, MLR and the VLR methods. The mean air temperature calculated with the VLR and MLR is similar on both sides, implying a reduction of 0.5 to 0.6°C relative to the ELR.

On the west side, ELR, VLR and MLR showed similar values, except on the tongues of the glaciers, where ELR shows mean air temperature over 10°C. The lowest mean air temperature is obtained with the SM10 method. SM10 shows a lower air temperature across all glacier surfaces, especially notable at the tongue of each of the glaciers. At the point scale, the comparison of the observed air temperature at GBL2 compared with the SM10 shows a mean difference of 0.6°C. This represents a reduction of the difference with the other methods (ELR, MLR and VLR) implying that SM10 captures some of the cooling effect of the glacier surface.

On the east side, the lowest mean air temperature is obtained with the VLRBias method. The SM10 just captures a small portion of the cooling effect as at the location of the GBL3, the mean difference with the observed data is only reduced by 0.1 °C compared with the difference using VLR. On both sides, some uncertainties exist in the magnitude of the real cooling effect using SM10 as we used the original parameters of Shea and Moore (2010) and not newly calibrated parameters.

On the east side, the difference between ELR/MLR and VLR is smaller along the plateau and the tongues of the glaciers. However, at higher elevations, the VLR determines warmer conditions due to the thermal inversion episodes. The vertical extension of the thermal inversion is an uncertainty, considering that there are no observations over ~1,500 m a.s.l., hence the data at higher elevations must be taken with caution.

On both sides the VLRBias air temperature distribution shows colder conditions compared with the ELR, MLR and the VLR. On the west side, the SM10 method gives higher cooling compared to VLRBias below 1,000 m a.s.l. and similar conditions in the range 1,000 to 1,500 m a.s.l. At higher elevations, SM10 shows warmer conditions than VLRBias. However, the area above 1,500 m a.s.l. is only ~10% of the total, which explains the generally colder conditions of SM10 compared to VLRBias on the west side (Figure 5). In the east, at the lower elevational range the

SM10 presents colder conditions compared with VLRBias; this is a small portion of the total area of the glaciers as their fronts are located at ~250-300 m a.s.l.

Spatially, the differences between the west and east side depend on the method used for the air temperature distribution. The ELR method determines almost the same condition for each elevation range between west and east, while the MLR and VLR method determine warm conditions on the east compared to the west in all the elevation ranges. The opposite is true using the VLRBias method with warmer conditions in the west up to ~2,000-2,500 m a.s.l. and then warmer conditions in the east due to the great number of thermal inversion episodes.

4.4 Ablation estimates

Hourly distributed degree-day modeling (DDM) shows the effects of the different air temperature distributions on estimating melt across the SPI during the period 1 October 2015 to 30 June 2016. For comparison, Figure 6 shows the differences in the melt between each of the methods used to distribute the air temperature. The differences are shown by elevation range and for a range of degree-day factors (DDFs).

In the west, the larger differences between all the methods are concentrated at elevations below 1,000 m a.s.l. The ELR melt is highest for most of the elevation range, except the greatest elevations where all the other methods tend to be similar or higher melt rate. The highest melt differences are between ELR/MLR-SM10, reaching values between 7 and 14 m w.e at the lower elevations. The VLR estimated greater melt than VLRBias, as expected; depending on the DDF used this difference could reach more than 3 m w.e. in the tongue of the glacier (0 to 1,000 m a.s.l.). However, with the typical DDF used for ice (6 to 7 mm w.e. $°C^{-1}$ d^{-1}), the difference is 1.5-2 m w.e. Interestingly, the differences between MLR-VLR are very low and the differences between VLRBias-SM10 are also low except at the very lower elevations, suggesting that greater cooling effect in the tongue of the glacier is represented by SM10. At the locations of GBL1 and GBL2 and over 1,000 m a.s.l. the differences are close to 0 m w.e.

On the east side, the VLR modeled melt is higher than the ELR at higher elevations and similar at lower elevations. Higher differences are observed in the lower sector between ELR-SM10, MLR-SM10, VLR-SM10, in all these cases with a maximum of 8 m w.e. assuming higher DDF. Differences between 4 to 6 m w.e. are observed for more typical DDF for ice (6 to 8 mm w.e. $°C^{-1}$ d^{-1}). The VLRBias-SM10 difference shows that the SM10 captures the cooling effect at the lower elevations, as the difference is close to 0 m w.e.

The results of the estimated melt using the five methods are compared with the observations of the ablation using UDGs at GBL1 and GBL2 locations (Table S2). The observed air temperatures at these locations, following the same DDM approach, suggest that the DDF to replicate the observed melt is close to 8.5 mm w.e. $°C^{-1}$ d^{-1}, which compares well with values derived in other glaciated areas (Hock, 2003). On both sides, ELR, MLR and VLR melt are higher than the observed; 0.4-0.5 m w.e. at GBL1 and 1.3 m w.e. at GBL2 location. VLRBias and SM10 melt rate are close to the observed values with an overestimation of 0.2-0.3 m w.e. at GBL2. This emphasizes that the inclusion of the cooling effect is necessary for melt estimations as this is a comparison with an independent source of data from the UDGs.

The results of the energy balance at point scale (Figure 7) show the spatial differences related to the meteorological conditions between the east side and the west side. Incoming shortwave radiation is higher in the east due to less humidity and cloud cover and incoming longwave radiation is slightly higher in the west due to more persistent cloud cover. Turbulent fluxes are the smaller contributors to the energy balance on both sides and are the most sensitive fluxes to the changes in the air temperature distribution method.

The sensitivity of the energy fluxes to three methods of air temperature distribution (VLR, VLRBias and SM10) are shown in Figures 7c and 7f. In the west, the greatest change is observed in energy available for melt, as the 208 W m^{-2} estimated by the VLR method reduces to 180 W m^{-2} (VLRBias) and 157 W m^{-2} (SM10). Refreezing values are similar. The mean latent heat changes from 45 W m^{-2} (VLR) to 24 W m^{-2} (VLRBias) and 19 W m^{-2} (SM10) and the sensible heat changes from 68 W m^{-2} (VLR) to 47 W m^{-2} (VLRBias) and 43 W m^{-2} (SM10). On the east side the changes in the turbulent fluxes are even higher; latent heat changes from 20 W m^{-2} (VLR) to -76 W m^{-2} (VLRBias) and 0 W m^{-2} (SM10) and the sensible heat changes from 91 W m^{-2} (VLR) to -24 W m^{-2} (VLRBias) and 70 W m^{-2} (SM10). The energy for melt also decreases from VLR to VLRBias, but increases comparing VLRBias and SM10.

The ablation impacts associated with the different methods to distribute the air temperature to input the point-scale energy balance are show in Figures 7c and 7f. The accumulated melt on the west side decreases from 7.4 m w.e (VLR) to 5.9 m w.e. (VLRBias) and 5.4 m w.e. (SM10), while sublimation increases from 0.03 m w.e. (VLR) to 0.05 m w.e. (VLRBias) and 0.04 m w.e. (SM10). In any case, these sublimation values represent a very small fraction (less than 0.8%) of the total melt. On the east side the differences are more evident, the accumulated melt decreases from 8.2 m w.e. (VLR) to 3.0 m w.e. (VLRBias) and 6.6 (SM10). The accumulated sublimation increases from 0.1 m w.e. (VLR and SM10) to 0.4 m w.e. (VLRBias). This means that in the east and using the VLRBias, sublimation comprises 12% of the total ablation. On the west side, a qualitative comparison of the ablation is obtained from UDGs data at GBL1 and GBL2. As GBL1 and GBL2 are located at higher elevation it is expected that the ablation will be lower with respect to the HSNO (1,040 m a.s.l.). Unfortunately, the UDG installed at GBL3 on the east side did not record data during the period of analysis. However, the UDG at GBL2 located at ~20 km from HSO represents an estimate, suggesting the VLRBias air temperature is closest to the observed ablation.

5 Discussion

5.1 Uncertainties

In estimating lapse rates from observations, it is important to recognize the influence that the number and position of stations may have on the derived values. For example, sites located at valleys bottoms, on mountain passes, and in positions elevated above glacier surfaces may not be representative of the wider terrain (Minder et al. 2010). In the current study, the correlation matrix of air temperatures revealed that GT and GO showed the weakest relationship. GT is located at the lower end of a small valley frequently affected by temperature inversion (Carturan et al., 2015). GO is located close to the front of the O’Higgins glacier, but in an area also affected by the wind dynamics of the valley of Pirámide glacier. Additionally, both AWSs are located close to water bodies, GT is close to a fjord and GO to a lake, and the boundary layer dynamics of these water bodies could also influence the air temperature at these locations. The great number of factors that potentially influence the air temperature observations indicate that corrections are necessary for using such data over glacier surfaces.

The reliability of on-glacier temperatures is crucial for the robustness of the VLRBias method. Our data show that GBL1 and GBL2 are well correlated with the observed air temperature at the nunataks (Table S1) and hence could be representative of the on-glacier conditions on the plateau of the west side. However, at GBL3, there is a greater uncertainty considering the short time series and the large-scale climate anomalies during this period, which were characterized by the predominance of high sea level pressure in fall (April to May) 2016 that brought about unusual weather conditions (Garreaud, 2018). Overall, correlation coefficients are lower between all the time series during the April-June period, especially when comparing rock AWS with nunatak AWS, with values around 0.01. However, the correlations between nunatak AWS (HSNO-HSG-HSO) are still between 0.88 and 0.94 which means that conditions on the plateau seem to be influenced in the same direction. This gives confidence that the GBL3 dataset, installed on the plateau, may reliably represent the long-term conditions on the east side of the SPI, or at least is representative of the cooling effect under sunny and warm conditions. These conditions were predominant in fall 2016 due to large-scale climate anomalies (Garreaud, 2018). This is also support by previous observations, as greater cooling effect has been observed under warm and sunny weather, while minimum values were observed during overcasts and unsettled weather (Carturan et al., 2015). However, the dispersion of the data, still suggests that local conditions exist at this point and hence the conditions may not be representative of all the glacier area. Probably, this is the main reason that the correlation coefficient in GBL3 (~0.60) is not as high as GBL1 and GBL2, at least when compared to nunatak AWS (>0.90).

5.2 Lapse rates and air temperature spatial patterns

Previous glacier mass balance modeling in the Patagonia region has not used spatial parametrization of LRs, but the results presented in this work demonstrate that clear spatial differences exist. Specifically, we show here that the observed LRs are low in the west relative to the east. Such differences across mountains are likely a common feature (e.g. the Cascade Mountains: Minder et al., 2010). At a smaller scale, there are also differences in the LRs observed between the lower and upper regions of the Icefield on both sides. Observed on-glacier LRs are lower than off-glacier LRs and the ELR, in agreement with findings for the Canadian Arctic (Marshall et al., 2007; Gardner and Sharp, 2009), but contrasting with steep LRs observed over valley glaciers in the Central Andes of Chile (e.g. Petersen and Pellicciotti, 2011; Bravo el al., 2017).

Despite their common use in modeling studies, our results suggest that while the ELR, MLR and VLR methods of temperature distribution do not represent the real on-glacier conditions, the VLR does appear to capture the on-glacier variability. Furthermore, the MLR captures the general spatial pattern and hence could also potentially be used.

For input to a glacier ablation model, including the glacier cooling effect in the air temperature distribution should theoretically give a more realistic estimate of the ablation. Considering that i) observed on-glacier lapse rates are difficult to obtain during longer periods, due to glacier surface characteristics (e.g. tilt of the structure by ice flux) and ii) that the correlations between observed and estimated air temperature over the glacier surface are good (Figure 4), the glacier cooling effect could be represented by a bias-correction (VLRBias, Equation 2) or by using the model of Shea and Moore (2010, SM10, Equation 3). However, for both cases, further on-glacier data would be useful for calibrating the approach. In the first case, it is necessary to include spatial differences between the on-glacier and off-glacier air temperatures, due to cold spots and different lateral conditions with respect to the centerlines that have been observed over other glaciers (Shaw et al., 2017). In the second case, further observations are needed to calibrate the parameters of the statistical model of Shea and Moore (2010), especially because the glaciers of the study area presents a longer fetch with respect to previous application on Alpine glaciers (e.g. Carturan et al., 2015; Shaw et al., 2017). An alternative to these corrections is the physically-based model that was proposed to capture on-glacier air temperature conditions under katabatic flow events developed by Greuell and Bohm (1998), applied by Petersen et al. (2013) and its modified version previously used by Ayala et al. (2015) and Shaw et al. (2017).

The dominant control of LRs depends of the size of the ice mass; Gardner et al. (2009) found that the free-atmosphere air temperature is the main control of the LRs rather than katabatic flow in icefields of the Canadian Arctic, but Petersen and Pellicciotti (2011) found that katabatic flow plays an important role in defining on-glacier air temperatures for a valley glacier. More in-depth analysis is therefore necessary to determine if katabatic flow plays an important role in the South Patagonia Icefield, and hence assess the applicability of the Greuell and Bohm (1998) and Shea and Moore (2010) models with greater confidence. The relationship between wind speed and LRs at the tongue of each side (LRs at GT-HSNO and GO-HSO, Figure S3) seems to suggest a control from katabatic flow especially on the east side due to the larger temperature gradient between surface and off-glacier conditions. However, the wind speed could also be related to synoptic conditions on both sides and strong foehn winds in the east, as was previously suggested by Ohata et al. (1985) in the North Patagonia Icefield, thus preventing the development of near continuous katabatic flow. Independent of the physical explanation it is clear that at the tongues, wind speed also plays a role in defining the variability of the LRs.

The meteorological conditions clearly play an important role in defining the characteristics of the LRs on both sides of the northern sector of the SPI. Shen et al. (2016) indicated that the role of water vapor in the air is an essential driver of the spatial pattern of LRs. Gentle LRs are associated with relatively moister atmospheric conditions, as rising air parcels cool more slowly in a humid environment than in a dry environment. Thus, the magnitude of temperature change with elevation is reduced. This mechanism can be revealed by the spatial variability of precipitation and humidity, which are higher on the western side than the eastern side as the meteorological observations and previous work indicates (Lenaerts et al., 2014; Schneider et al., 2003; Smith and Evans, 2007).

LR variability also depends on atmospheric circulation patterns. For example, the observed LRs in the area show episodes of thermal inversions, particularly in the fall months. These episodes respond to atmospheric circulation that favor the advection of warm air to the South Patagonia Icefield (Garreaud, 2018). During these episodes, on the west side, negative LRs were observed on the plateau, while positive LRs were observed on the tongues. At the end of April, the air temperature at HSNO and HSG increased, reaching positive values during this period. Meanwhile, GT does not show this increase (Figure 2). This could indicate that the air temperature close to the glacier surface does not rise uniformly and the air temperature at higher elevation responds more linearly to a free-air temperature increase, as was previously suggested by Gardner et al. (2009).

It is generally accepted that at the regional scale, relatively colder air temperatures prevail on the eastern side compared to the west side over both Patagonia Icefields (Garreaud et al., 2013;

Villarroel et al., 2013), related to the topographic elevation differences between both flanks. However, at similar elevations, the use of VLR and the off-glacier observations near the front of the glaciers (GT and GO) seem to describe warmer conditions in the east compared to the west, but a steeper LR on the east, in apparent support of the results of Mernild et al. (2016).

5.3 Glacier cooling effect

On-glacier air temperature measurements reveal that the cooling effect associated with the glacier surface is higher in the east. Observed mean glacier cooling reaches a maximum of 3.3 °C relative to the VLR extrapolated between neighbouring stations at the location of the GBL3 on the east side and under severe drought conditions in Patagonia (Garreaud, 2018). Similar magnitudes (3 °C to 4 °C) were previously observed at the Skagastøl Glacier (Norway) by Erikkson (1958) (in Carturan et al., 2015) and in Juncal Norte glacier in Central Chile (~33°S), where Ragettli et al. (2013) found a cooling effect of 2.9°C. However, the values of the k_1 and k_2 parameters at GBL3 suggests a strong cooling effect besides been locate close to the ridge (Figure S1). The curves of Shea and Moore (2010) and Shaw et al. (2017) suggests that the cooling effect at this point must be low. This discrepancy could be explained if the location of GBL3 is a cold spot. These special features require further investigation as the models cannot replicate (Shaw et al., 2017). Meanwhile, at GBL1 and GBL2, located on the west side, the cooling was between 0.8°C and 1.3°C. Although the one point of on-glacier validation and the extension of the GBL3 time series is insufficient to define the real cooling effect and its spatial differences, previous work suggests that the east side of the SPI is indeed cooler than the west. Monahan and Ramage (2010) used passive microwave observations to show that the melt-refreeze processes below 1,500 m a.s.l. start in July on the western part of the SPI, while in the east they start in September; sustained melt onset also tends to occur 25 to 35 days earlier on the west of the divide than in the east. De Angelis et al. (2007) showed larger areas of slush in the west compared to the east, as well as a greater degree of snow metamorphism associated with melt-freeze episodes in the west, suggesting relatively warmer conditions.

The SM10 method also suggests slightly colder on-glacier conditions in the east compared to the west, but limited to the elevation range between 1,000-2,000 m a.s.l., where 80% of the glacier area is concentrated. At the other elevation ranges, SM10 shows warmer on-glacier conditions in the east. This spatial variability reinforces the need for more distributed and longer term on-glacier observations.

5.4 Ablation impacts

There is an evident impact in the reduction of the melt using a DDM with the VLRBias and SM10 air temperature dataset compared to the DDM using the ELR, MLR and VLR air temperatures. At point scale, these differences are higher in the east reaching values between 4 to 6 m w.e. for DDFs between 6 and 9 mm w.e. $°C^{-1}$ d^{-1} at 500 m a.s.l. Assuming the mean annual melt of ~10-12 m w.e. for the tongue of O'Higgins glacier, estimated by Mernild et al. (2016), the difference between the methods represents between 33% and 60% of the melt at point scale. At the distributed scale, the mean melt in the period 1979/80 and 2013/14 estimated by Mernild et al. (2016) reached a mean value of 8.1 m w.e. on the west side (Greve, Tempano and Occidental glaciers) and 6.3 m w.e. on the east side (O'Higgins and Chico glaciers). Although there are some restrictions in comparing these data (mean of 30 years) and the results of the current study (one particular season and an estimated DDF of 8.5 mm w.e. °C^{-1} d^{-1}), it appears that in the east, the melt determined by Mernild et al. (2016) is too high even compared with the melt obtained from the ELR and MLR (5.6 and 5.9 m w.e.) while in the west the value obtained by Mernild et al. (2016) is close to our VLRBias estimation.

Overall, the use of the constant ELR, MLR and VLR appears to overestimate the melt calculated by a DDM. However, MLR and VLR describe the variability of the on-glacier air temperature and hence could be used, after a correction, to estimate the melt. As the MLR represents the general spatial conditions (east-west; tongue-plateau), it should be noted that the MLR does not capture thermal inversion episodes and could underestimate the melt/ablation at higher elevations. The use of VLR has been highlighted as an important issue in glaciology applications (Marshall et al., 2007; Petersen and Pellicciotti, 2011).

The point-scale energy balance showed that the energy available decreases from VLR to VLRBias and SM10, hence, the melt decreases, notably on the east side. The energy balance results highlight that the most important impacts on the energy balance are related to the change in the sign of the turbulent fluxes using the VLRBias compared to the VLR as input to the energy balance model on the east side. The sublimation here, after a change in the sign of the mean latent heat, reaches 12% of the total ablation at 1,234 m a.s.l. This percentage could be even larger at higher elevations on the east side. Overall, the sublimation is considered a small percentage of the total ablation with values in the order of 0.1 m w.e. for the glaciers of the study area (Mernild et al., 2016). However, if the cooling effect is as high as the data from GBL3 suggest, the sublimation on the east side could be higher and hence attention must be given to this ablation component when modelling future climate response.

Although the data in the current study are not conclusive, it does appear that spatially variable cooling effects must be considered as an important control on the differential response of the glaciers in this region, which has previously been attributed to the hypsometric characteristics and calving dynamics (e.g. De Angelis, 2014; Minowa et al., 2015; Rivera et al, 2014).

6 Conclusions

This work presents air temperature variations across the South Patagonia Icefield (SPI) along an east-west transect at approximately 48° 45’ S. We analyzed nine months of observations from a network of five complete series of automatic weather stations (AWSs) installed close to glacier fronts and on nunataks, supplemented by three air temperature sensors installed directly over the glacier surface. By analyzing these time series of observed air temperature and distributed values modeled with the observed lapse rates, including a bias-correction over glacier surfaces, we identified spatial variability in the air temperature structure between the east and the west sides of the icefield. This work represents the first robust assessment of air temperature variability on the SPI. The main findings are as follows:

1. There is considerable spatial and temporal variability in LRs. Observed lapse rates are, overall, steeper in the east (-0.0072 °C m^{-1}) compared to the west (-0.0055 °C m^{-1}) and also differences and even contrasting behavior in the LRs exist between the lower sections (tongue of glacier, ablation zone) and upper sections (plateau, accumulation zone) on each side of the SPI. In the west, the mean LR at the tongue (GT-HSNO) reached -0.0045 °C m^{-1} while at the plateau

(HSNO-HSG) it reached -0.0064 °C m^{-1}. In the east, mean LR reached -0.0066 °C m^{-1} at the tongue (GO-HSO) and -0.0078 °C m^{-1} at the plateau (HSO-HSG).

2. Off-glacier temperature measurements are not representative for calculating on-glacier LRs. While off-glacier LR accounts for the variability of the on-glacier air temperature, a bias exists in comparing the estimated and the observed air temperature time series. Applying a bias-correction and/or the model of Shea and Moore (2010), we find that on-glacier conditions are warmer on the west side compared to the east. The methods to distribute air temperature could reach differences of ~1°C in the west and 3.3°C in the east when comparing mean values. At the local scale, differences reach values higher than 10°C especially on the tongues at each side. Certainly, more on-glacier measurements are needed to account for this effect at the scale of the entire icefield.

3. These two factors (1 and 2) have an impact on ablation estimates. Investigating the sensitivity of ablation to modeled air temperatures shows that important differences exist depending on the method used for air temperature distribution. Distributed temperature-index modeling and point-scale energy balance analysis reveal that melt could be overestimated and sublimation could be underestimated if the glacier cooling effect is not included in the distributed temperature data. These uncertainties can lead to large variations in the estimated ablation. Overall, on the east side, total melt without air temperature corrections (ELR, MLR and VLR) decreases by 51-56% for bias-corrected air temperatures (VLRBias) and 13-22% for the model of Shea and Moore (2010). On the west side, this decrease is 21-31% and 54-60%, respectively. At the local scale, the energy balance shows that in the east (HSO), a reduction of 59% exists in the total ablation between VLR and VLRBias and a reduction of 19% exists between VLR and SM10. In the west (HSNO) this reduction is 20% and 27%, respectively. The turbulent flux analysis also shows that with the greater glacier cooling effect on the east side, sublimation could reach 12% of the total ablation.

In view of these findings, the main implication is that using a single, constant LR value for both sides to distribute the air temperature, is not representative. Considering the overall, strong correlation between air temperature time series, the use of VLR captures the on-glacier variability. Also, the use of MLR captures the general spatial different conditions and hence could be used. However, for both cases, including the glacier cooling effect in the air temperature distribution gives more reliable ablation estimations. The correction could be done by a bias-corrections as was proposed here (VLRBias), using the model of Shea and Moore (2010, SM10) or by testing the applicability of other models (e.g. Greuell and Bohm, 1998). The calculation of the surface mass balance in these glaciers and others could be improved considering the spatial differences in the observed lapse rate and taking account of the cooling effect to distribute the air temperatures.

Acknowledgments

We acknowledge the DGA for providing their data for analysis (http://www.dga.cl/Paginas/estaciones.aspx). CECs provided all the logistical support in four field campaigns. A. Rivera was supported by FONDECYT 1171832 and CECs. C. Bravo acknowledges support from the CONICYT Becas-Chile PhD scholarship program. We would like to thank Federico Cazorzi and the anonymous reviewers for their constructive and useful comments and recommendations.

References

Aniya, M., Sato, H., Naruse, R., Skvarca, P. and Casassa, G. (1996), The use of satellite and airborne imagery to inventory outlet glaciers of the Southern Patagonia Icefield, South America. Photogrammetric Engineering and Remote Sensing, 62(12), 1361–1369.

Ayala, A., Pellicciotti, F. & Shea, J.M. (2015), Modeling 2 m air temperatures over mountain glaciers: exploring the influence of katabatic cooling and external warming. Journal of Geophysical Research: Atmospheres, 120, 1–19.

Ayala, A., Pellicciotti, F., MacDonell, S., McPhee, J., Vivero, S., Campos, C. & Egli, P. (2016), Modelling the hydrological response of debris-free and debris-covered glaciers to present climatic conditions in the semiarid Andes of central Chile, Hydrological Processes, 30, 4036–4058, https://doi.org/10.1002/hyp.10971.

Barry, R.G. (2008), Mountain Weather and Climate, Cambridge: University Press Cambridge.

Bliss, A., Hock, R. & Radić, V. (2014), Global response of glacier runoff to twenty-first century climate change, Journal of Geophysical. Research: Earth Surface, 119, 717–730, doi:10.1002/2013JF002931

Bolton, D. (1980), The computation of equivalent potential temperature. Monthly Weather Review, 108, 1046–1053.

Bravo, C., Rojas, M., Anderson, B.M, Mackintosh, A.N., Sagredo, E., & Moreno, P.I. (2015), Modelled glacier equilibrium line altitudes during the mid-Holocene in the southern mid-latitudes. Climate of the Past, 11, 1575 – 1586.

Bravo, C., Loriaux, T., Rivera, A., & Brock, B.W. (2017), Assessing glacier melt contribution to streamflow at Universidad Glacier, central Andes of Chile. Hydrological and Earth System Science, 21, 3249-3266.

Brock, B. & Arnold, N. (2000), A spreadsheet-based (Microsoft Excel) point surface energy balance model for glacier and snowmelt studies. Earth Surface Processes and Landforms, 25, 649-658.

Brock, B. W., Willis, I. C., & Sharp, M. J. (2006), Measurement and parameterization of aerodynamic roughness length variations at Haut Glacier D'Arolla, Switzerland. Annals of Glaciology, 52, 281–297.

Carrivick, J.L., Davies, B.J., James, W.H.M., Quincey, D.J., & Glasser, N.F. (2016), Distributed ice thickness and glacier volume in southern South America. Global and Planetary Change, 146, 122-132.

Carturan, L., Cazorzi, F., De Blasi, F. & Dalla Fontana, G. (2015), Air temperature variability over three glaciers in the Ortles–Cevedale (Italian Alps): effects of glacier fragmentation, comparison of calculation methods, and impacts on mass balance modeling. The Cryosphere, 9, 1129–1146.

CECs-DGA (2016), Línea de base glaciológica del sector norte de Campo de Hielo Sur: Glaciares Jorge Montt, Témpano y O'Higgins. SIT N° 404, DGA, Technical Report in Spanish.

Cook, K., Yang, X., Carter, C., & Belcher, B. (2003), A modelling system for studying climate controls on mountain glaciers with application to the Patagonian Icefields. Climatic Change, 56, 339 – 367.

Cuffey, K. M. & Paterson, W. S. B. (2010), The Physics of Glaciers, 4th ed., Oxford: Elsevier.

Davies, B.J., Golledge, N.R., Glasser, N.F., Carrivick, J.L., Ligtenberg, S.R., Barrand, N.E., Van Den Broeke, M.R., Hambrey, M.J. & Smellie, J.L. (2014), Modelled glacier response to centennial temperature and precipitation trends on the Antarctic Peninsula, Nature Climate Change, 4, 993-998, doi: 10.1038/nclimate2369

Davies, B.J., & Glasser, N.F. (2012), Accelerating shrinkage of Patagonian glaciers from the Little Ice Age (similar to AD 1870) to 2011. Journal of Glaciology, 58, 1063-1084.

De Angelis, H., Rau, F., & Skvarca, P. (2007), Snow zonation on Hielo Patagónico Sur, southern Patagonia, derived from Landsat 5 TM data. Global and Planetary Change, 59, 149–158.

De Angelis, H. (2014), Hypsometry and sensitivity of the mass balance to change in equilibrium-line altitude: the case of the Southern Patagonia Icefield. Journal of Glaciology, 60, 14 – 28.

Ebrahimi, S. & Marshall, S. J. (2016), Surface energy balance sensitivity to meteorological variability on Haig Glacier, Canadian Rocky Mountains. The Cryosphere, 10, 2799-2819.

Foresta, L., Gourmelen, N., Weissgerber, F., Nienow, P., Williams, J.J., Shepherd, A., Drinkwater, M.R. & Plummer, S. (2018), Heterogeneous and rapid ice loss over the Patagonian Ice Fields revealed by CryoSat-2 swath radar altimetry, Remote Sensing of Environment, 2018, 441-455, doi.org/10.1016/j.rse.2018.03.041.

Gardner, A. S., & Sharp, M.J. (2009), Sensitivity of net mass-balance estimates to near-surface temperature lapse rates when employing the degree-day method to estimate glacier melt. Annals of Glaciology, 50, 80–86.

Gardner, A. S., Sharp, M. J., Koerner, R. M., Labine, C., Boon, S., Marshall, S. J., Burgess D.O., & Lewis, D. (2009), Near-surface temperature lapse rates over arctic glaciers and their implications for temperature downscaling. Journal of Climatology, 22, 4281–4298. doi:10.1175/2009JCLI2845.1.

Gardner, A.S., Moholdt, G., Cogley, J.G., Wouters, B., Arendt, A.A., Wahr, J., Berthier, E., Hock, R., Pfeffer, W.T., Kaser, G., Ligtenberg, S.R.M., Bolch, T., Sharp, M.J., Hagen, J.O., van den Broeke, M.R., Paul, F., (2013), A reconciled estimate of glacier contributions to sea level rise: 2003 to 2009. Science 340 (6134), 852–857, doi.org/10.1126/science.1234532.

Garreaud, R. (2018), Record-breaking climate anomalies lead to severe drought and environmental disruption in Western Patagonia in 2016. Climate Research, 74, 217-229, doi.org/10.3354/cr01505.

Garreaud, R., Lopez, P., Minvielle, M., & Rojas, M. (2013), Large-Scale control on the Patagonian Climate. Journal of Climate, 26, 215 – 230.

Gourlet, P., Rignot, E., Rivera, A., & Casassa, G. (2016), Ice thickness of the northern half of the Patagonia Icefields of South America from high-resolution airborne gravity surveys. Geophysical Research Letters, 43, 241-249. doi:10.1002/2015GL066728.

Greuell, W., & Böhm, R. (1998), 2m temperatures along melting midlatitude glaciers, and implications for the sensitivity of the mass balance to variations in temperature. Journal of Glaciology, 44(146), 9–20.

Greuell W., & Genthon, C., (2003), Modelling land ice surface mass balance. In Bamber, J.L. and A.J. Payne, eds. Mass balance of the cryosphere: observations and modelling of con- temporary and future changes. Cambridge, Cambridge University Press.

Hanna, E., Mernild, S., Yde, J.C., & de Villiers, S. (2017), Surface air temperature fluctuations and lapse rates on Olivares Gamma glacier, Rio Olivares basin, Central Chile, from a novel meteorological sensor network. Advances in Meteorology, 2017, 1-15, doi:10.1155/2017/6581537

Heynen, M., Pellicciotti, F., & Carenzo, M. (2013), Parameter sensitivity of a distributed enhanced temperature-index melt model. Annals of Glaciology, 54(63), 311-321. doi:10.3189/2013AoG63A537

Heynen, M., Miles, E., Ragettli, S., Buri, P., Immerzeel, W., & Pellicciotti, F. (2016), Air temperature variability in a high-elevation Himalayan catchment. Annals of Glaciology, 57 (71), 212–222.

Hock, R. (2003), Temperature index melt modelling in mountain regions. Journal of Hydrology, 282, 104–115.

Hock, R. (2005), Glacier melt: a review of processes and their modelling. Progress in Physical Geography, 29, 362–391.

Immerzeel, W.W., Petersen, L., Ragettli, S. & Pellicciotti, F. (2014), The importance of observed gradients of air temperature and precipitation for modeling runoff from a glacierised watershed in the Nepalese Himalayas. Water Resource Research, 50, 2212–2226.

Kerr, A., & Sugden, D. (1994), The sensitivity of the southern Chilean snowline to climatic change. Climatic Change, 28, 255 – 272.

Lenaerts, J.T.M., van den Broeke,M.R., van Wessem, J.M., van de Berg, W.J., van Meijgaard, E., van Ulft, L., & Schaefer, M. (2014), Extreme Precipitations and Climate Gradients in Patagonia Revealed by High-Resolution Regional Atmospheric Climate Modeling. Journal of Climate, 27, 4607-4621.

Liston G. E., & Elder K. (2006), A meteorological distribution system for high-resolution terrestrial modeling (MicroMet). Journal of Hydrometeorology, 7, 217–234. doi: 10.1175/JHM486.1

Mackay, J. D., Barrand, N. E., Hannah, D. M., Krause, S., Jackson, C. R., Everest, J., & Aðalgeirsdóttir, G. (2018), Glacio-hydrological melt and run-off modelling: application of a limits of acceptability framework for model comparison and selection. The Cryosphere, 12, 2175-2210, https://doi.org/10.5194/tc-12-2175-2018.

Malz, P., Meier, W., Casassa, G., Jaña, R., Skvarca, P., & Braun, M.H. (2018), Elevation and Mass Changes of the Southern Patagonia Icefield Derived from TanDEM-X and SRTM Data. Remote Sensing, 10(2), 188. doi:10.3390/rs10020188

Masiokas, M., Villalba, R., Luckman, B., Lascano, M., Delgado, S., & Stepanek, P. (2008), 20th-century glacier recession and regional hydroclimatic changes in northwestern Patagonia. Global and Planetary Change, 60, 85–100

Marshall, S. J., Sharp, M. J., Burgess, D. O., & Anslow, F. S. (2007), Near-surface temperature temperature gradients on the Prince of Wales Icefield, Ellesmere Island, Canada: implications for regional downscaling of temperature. International Journal of Climatology, 27, 385–398.

Meier, W.J-H, Grießinger, J., Hochreuther, P. & Braun, M.H. (2018), An Updated Multi-Temporal Glacier Inventory for the Patagonian Andes With Changes Between the Little Ice Age and 2016. Frontiers in Earth Science, 6, doi: 10.3389/feart.2018.00062

Mernild, S. H., Liston, G. E., Hiemstra, C. A., & Wilson, R. (2016), The Andes Cordillera. Part III: Glacier Surface Mass Balance and Contribution to Sea Level Rise (1979–2014). International Journal of Climatology, 37, 3154–3174.

Minder, J.R., Mote, P.W., & Lundquist, J.D. (2010), Surface temperature temperature gradients over complex terrain: lessons from the Cascade Mountains. Journal of Geophysical Research, 115, D14122. doi: 101029/2009JD013493.

Minowa, M., Sugiyama, S., Sakakibara, D., & Sawagaki, T. (2015), Contrasting glacier variations of Glaciar Perito Moreno and Glaciar Ameghino, Southern Patagonia Icefield. Annals of Glaciology, 56, 26–32.

Monahan, P. & Ramage, J. (2010), AMSR-E Melt Patterns on the Southern Patagonian Icefield. Journal of Glaciology, 56, 699-708.

NASA JPL (2013), NASA Shuttle Radar Topography Mission Global 3 arc second sub-sampled [Data set]. NASA EOSDIS Land Processes DAAC. doi: 10.5067/MEaSUREs/SRTM/SRTMGL3S.003

Oerlemans, J. (2001), Glaciers and Climate Change, Rotterdam, Netherlands: A. A. Balkema.

Ohata T., Kobayashi, S., Enomoto, H., Kondo, H., Saito, T., & Nakajima, C. (1985), The east-west contrast in meteorological conditions and its effect on glacier ablation. Bulletin of Glaciological Research, 3, 52-53.

Oke, T. R. (1987), Boundary Layer Climate, 2nd ed., London: Methuen.

Pellicciotti, F., Brock, B., Strasser, U., Burlando, P., Funk, M., & Corripio, J. (2005), An enhanced temperature-index glacier melt model including the shortwave radiation balance: development and testing for Haut Glacier d'Arolla, Switzerland. Journal of Glaciology, 51(175), 573–587. doi.org/10.3189/172756505781829124

Pellicciotti, F., Ragettli, S., Carenzo, M., & McPhee, J. (2014), Changes of glaciers in the Andes of Chile and priorities for future work. Science of the Total Environment, 493, 1197-1210, doi.org/10.1016/j.scitotenv.2013.10.055

Petersen, L. & Pellicciotti, F. (2011), Spatial and temporal variability of air temperature on a melting glacier: atmospheric controls, extrapolation methods and their effect on melt modeling, Juncal Norte Glacier, Chile. Journal of Geophysical Research, 116, D23109. doi: 10.1029/2011JD015842

Petersen, L., Pellicciotti, F., Juszak, I., Carenzo, M. & Brock, B.W. (2013), Suitability of a constant air temperature lapse rate over an alpine glacier: testing the Greuell and Böhm model as an alternative. Annals of Glaciology, 54, 120–130.

Popovnin, V., Danilova, T., & D. Petrakov, D. (1999), A pioneer mass balance estimate for a Patagonian glacier: Glaciar De Los Tres, Argentina. Global and Planetary Change, 22: 255 – 267.

Radić, V., Bliss, A., Beedlow, A. C., Hock, R., Miles, E., & Cogley J.G. (2013), Regional and global projections of 21st century glacier mass changes in response to climate scenarios from global climate models, Climate Dynamics, 42, 37–58, doi:10.1007/s00382-013-1719-7.

Ragettli, S., Cortés, G., McPhee, J. & Pellicciotti F. (2014), An evaluation of approaches for modelling hydrological processes in high-elevation, glacierized Andean watersheds. Hydrological Processes, 28, 5674–5695, doi:10.1002/hyp.10055

Rignot, E., Rivera, A., & Casassa, G. (2003), Contribution of the Patagonia Icefields of South America to Sea Level Rise. Science, 302, 434-436, 2003.

Rivera, A. (2004), Mass balance investigations at Glaciar Chico, Southern Patagonia Icefield, Chile (Doctoral dissertation), University of Bristol, UK.

Rivera, A.; Corripio, J., Bravo, C. & Cisternas, S. (2012), Glaciar Jorge Montt (Chilean Patagonia) dynamics derived from photos obtained by fixed cameras and satellite image feature tracking. Annals of Glaciology, 53(60), 147-155.

Sagredo, E., & Lowell, T. (2012), Climatology of Andean glaciers: A framework to understand glacier response to climate change. Global and Planetary Change, 86 – 87, 101 – 109.

Sakakibara, D., & Sugiyama, S. (2014), Ice-front variations and speed changes of calving glaciers in the Southern Patagonia Icefield from 1984 to 2011. Journal of Geophysical Research: Earth Surface, 119, 2541–2554. doi:10.1002/2014JF003148

Schaefer, M., Machguth, H., Falvey, M., & Casassa, G. (2013), Modeling past and future surface mass balance of the Northern Patagonian Icefield. Journal of Geophysical Research: Earth Surface, 118, 571–588. doi:10.1002/jgrf.20038

Schaefer, M., Machguth, H., Falvey, M., Casassa, G., & Rignot, E. (2015), Quantifying mass balance processes on the Southern Patagonia Icefield. The Cryosphere, 9, 25–35.

Schneider, C., Glaser, M., Killian, R., Santana, A., Butorovic, N., & Casassa, G. (2003), Weather observations across the Southern Andes at 53°S. Physical Geography, 24, 97-119.

Shaw, T., Brock, B. W., Fyffe, C., Pellicciotti, F., Rutter, N. & Diotri, F. (2016), Air temperature distribution and energy-balance modelling of a debris-covered glacier, Journal of Glaciology, 62, 185–198.

Shaw, T. E., Brock, B. W., Ayala, A., Rutter, N., & Pellicciotti, F. (2017), Centreline and cross-glacier air temperature variability on an Alpine glacier: Assessing temperature distribution methods and their influence on melt model calculations. Journal of Glaciology, 63(242), 973–88.

Shea, J. M. & Moore, R. D. (2010), Prediction of spatially distributed regional-scale fields of air temperature and vapour pressure over mountain glaciers, Journal of Geophysical Research, 115, D23107. doi:10.1029/2010JD014351

Shen, Y. J., Shen, Y., Goetz, J., & Brenning, A. (2016), Spatial-temporal variation of near-surface temperature lapse rates over the Tianshan Mountains, central Asia. Journal of Geophysical Research: Atmospheres, 121, 14006–14017. doi:10.1002/2016JD025711

Smith, R., & Evans, J. (2007), Orographic precipitation and water vapor fractionation over the Southern Andes. Journal of Hydrometeorology, 8, 3 – 19.

Stuefer, M., Rott, H., & Skvarca P. (2007), Glaciar Perito Moreno, Patagonia: climate sensitivities and glacier characteristics preceding the 2003/04 and 2005/06 damming events. Journal of Glaciology, 53(180), 3–16. doi: 10.3189/172756507781833848

Takeuchi, Y., Naruse R. & Skvarca, P. (1996), Annual air-temperature measurement and ablation estimate at Moreno Glacier, Patagonia, Bulletin of Glacier Research, 14, 23-28.

Teutschbein, C., & Seibert, J. (2012), Bias Correction of Regional Climate Model Simulations for Hydrological Climate-Change Impact Studies: Review and Evaluation of Different Methods. Journal of Hydrology, 456-457, 11-29.

Tsai, V., & Ruan, X. (2018). A simple physics-based improvement to the positive degree day model. Journal of Glaciology, 1-8. doi:10.1017/jog.2018.55

Villarroel, C., Carrasco, J., Casassa, G., & Falvey, M. (2013), Modeling near-surface air temperature and precipitation using WRF with 5-km resolution in the Northern Patagonia Icefield: A pilot simulation. International Journal of Geosciences, 4, 1193–1199. doi:10.4236/ijg.2013.48113

Warren, C., & Sugden, D. (1993), The Patagonian Icefields: A glaciological review. Arctic and Alpine Research, 25(4), 316-331.

Weidemann, S.S., Sauter, T., Malz, P., Jaña, R., Arigony-Neto, J., Casassa, G., & Schneider, C. (2018), Glacier Mass Changes of Lake-Terminating Grey and Tyndall Glaciers at the Southern Patagonia Icefield Derived From Geodetic Observations and Energy and Mass Balance Modeling. Frontiers in. Earth Science, 6, doi: 10.3389/feart.2018.00081

Wheler, B. A., Macdougall, A. H., Petersen, E. I., & Kohfeld, K. E. (2014), Effects of temperature forcing provenance and extrapolation on the performance of an empirical glacier-melt model. Arctic Antarctic and Alpine Research, 46, 379–393.

White, A., & Copland, L. (2015), Decadal-scale variations in glacier area changes across the Southern Patagonian Icefield since the 1970s. Arctic Antarctic and Alpine Research, 47, 147–167, 2015.

Willis, M., Melkonian, A., Pritchard, M., & Rivera, A. (2012), Ice loss from the Southern Patagonian Ice Field, South America, between 2000 and 2012. Geophysical Research Letters, 39, L17501. doi:10.1029/2012gl053136

Wilson, R., Carrión, D., & Rivera, A. (2016), Detailed dynamic, geometric and supraglacial moraine data for Glaciar Pio XI, the only surge-type glacier of the Southern Patagonia Icefield. Annals of Glaciology, 57,119-130.

Table 1. Details of the location, period of measurements and sensor characteristics of the five AWSs and the three GBL stations. The name of each AWS is the official name given by the DGA (www.dga.cl).

Location		**Automatic Weather Station**	**Acronym**	**Latitude / Longitude / [m a.s.l.]**	**Air temp. sensors**	**Error**	**Height [m]**	**Period**
West	Rock	Glaciar Témpano	GT	48°42'09"S/ 73°59'17'W/ 50	Young 41382VC	±0.3°C at 23°C	2	1 October 2015 - 30 June 2016
West	Nunatak	Hielo Sur en Glaciar Greve, Nunatak Occidental	HSNO	48°49'59"S/ 73°43'25"W/ 1040	Rotronic HC2-S3	±0.1°C at 23°C	2	1 October 2015 - 30 June 2016
West	Nunatak	Hielo Sur en Glaciar Greve	HSG	48°49'55"S/ 73°34'53"W/ 1428	Young 41382VC	±0.3°C at 23°C	2	1 October 2015 - 30 June 2016
West	Glacier surface	Glacier Boundary Layer Station 1	GBL1	48°50'02"S/ 73°34'51"W/ 1415	Thermistor 107-L	±0.2°C - ±0.5°C	1.2	17 October 2015 - 15 February 2016
West	Glacier surface	Glacier Boundary Layer Station 2	GBL2	48°51'34"S/ 73°31'37"W/ 1294	Thermistor 107-L	±0.2°C - ±0.5°C	2	25 October 2015 - 31 March 2016
East	Glacier surface	Glacier Boundary Layer Station 3	GBL3	48°54'30"S/ 73°27'47"W/ 1378	Thermistor 109-L	±0.1°C - ±0.5°C	2	10 April 2016 -30 June 2016
East	Nunatak	Hielo Sur en Glaciar O'Higgins	HSO	48°55'28"S/ 73°16'26"W/ 1234	Rotronic HC2-S3	±0.1°C at 23°C	2	17 October 2015 - 30 June 2016
East	Rock	Glaciar O´Higgins	GO	48°55'47"S/ 73°08'21'W/ 310	Young 41382VC	±0.3°C at 23°C	2	1 October 2015 - 30 June 2016

Table 2. Mean seasonal lapse rate at hourly time step for each season. Spring is October to December, summer is January to March and fall April to June. Number of cases are indicated by n and number of thermal inversions episodes (abbreviation t.i.) in brackets. The table include data from multi-linear regression of air temperature observations against elevation where parenthesis indicate the R^2 relationship. Also data obtained between each pair of AWS is showed (stepwise).

	Multi-site linear regression						**Stepwise**							
							West				**East**			
	All AWSs		**All AWSs West**		**All AWSs East**		**GT-HSNO**		**HSNO-HSG**		**GO-HSO**		**HSO-HSG**	
Season	n (t.i.)	Lapse rate [°C m^{-1}] (R^2)	n (t.i.)	Lapse rate [°C m^{-1}] (R^2)	n (t.i.)	Lapse rate [°C m^{-1}] (R^2)	n (t.i.)	Lapse rate [°C m^{-1}]	n (t.i.)	Lapse rate [°C m^{-1}]	n (t.i.)	Lapse rate [°C m^{-1}]	n (t.i.)	Lapse rate [°C m^{-1}]
Spring	1672 (7)	-0.0074 (0.97)	2024 (16)	-0.0066 (0.99)	1672 (2)	-0.0081 (0.99)	2208 (36)	-0.0066	2208 (17)	-0.0068	1824 (14)	-0.0080	1672 (46)	-0.0092
Summer	1998 (89)	-0.0069 (0.93)	1971 (84)	-0.0059 (0.99)	2002 (85)	-0.0077 (0.99)	2180 (115)	-0.0058	2180 (47)	-0.0065	2184 (164)	-0.0077	2002 (75)	-0.0082
Fall	1993 (428)	-0.0028 (0.61)	1993 (471)	-0.0029 (0.86)	2002 (320)	-0.0048 (0.98)	2175 (732)	-0.0020	2175 (77)	-0.0060	2184 (397)	-0.0046	2002 (341)	-0.0064

Figure 1. a) Spatial configuration of the AWSs (red triangles) and Ultrasonic depth gauges (GBL1, GBL2 and GBL3). Glacier contours (blue lines) are from De Angelis (2014). Purple line is the profile in b). The satellite image is a Landsat from the 8 April 2014. Contour lines are 400 m spaced. b) Longitudinal profile of the elevations of AWS and Sonic Ranges. Bedrock topography is derived from thickness observed data from Gourtel et al. (2015, black line) and thickness modelled data from Carrivick et al. (2016, green line). Dashed black line represents the ice divide.

Figure 2.a) Time series of the mean daily temperature of the five AWS and the three snow sensors. Sensors are located 2 m above the ground, except GBL1 located at 1.2 m. Grey shadows correspond to the minimum and maximum values in each day. The order from top to bottom is from west to east. Note that y-axis is different between plots. b) Hourly mean for each AWSs for the period 25-Oct-2015 to 15-Feb-2016 and c) Hourly mean for each AWSs for the period 10-Oct-2016 to 30-Jun-2016.

Figure 3. Monthly boxplot of the LRs estimated for each pair of AWS. Upper and lower box limits are the 75% and 25% quartiles, the red horizontal line is the median, the filled green circle is the mean, and crosses are outlying values. As a reference, the ELR and the dry adiabatic lapse rate are indicated. For panel e) note the different y-axis scale (dashed lines correspond to the range in all other panels). The grey line corresponds to zero lapse rate.

Figure 4. Scatter plot of the observed air temperature and the estimated air temperature using the VLR method. Locations are a) GBL1, b) GBL2 and c) GBL3. Colored according to the relative humidity observed at HSG. Black line is the best fit and the dashed line is the one-to-one relation.

Figure 5. Mean air temperature for each method for distribute the air temperature on both sides of the SPI. Color bar units are °C. Elevation contour lines interval 200 m. The top row shows the west side and the bottom row the east side.

Figure 6. Melt differences between each of the methods used to distribute the air temperature using a range of DDF in a simple degree-day model. Upper panels correspond to the west side and lower panels to the east side. Note that at east side the lowest elevation is 250 m a.s.l.

Figure 7. Results of the point-scale energy balance: a) Estimated mean energy fluxes using different air temperature distributions schemes; b) Observed radiation fluxes; c) Estimated cumulative melt and sublimation and observed ablation at GBL1 and GBL2 locations; Shadowed area corresponds to the range of snow densities observed at both locations. a), b) and c) are on the west side at the location of HSNO. d), e) and f) are on the east side at the location of HSO. Note that in panels c) and f) sublimation are on different scales.

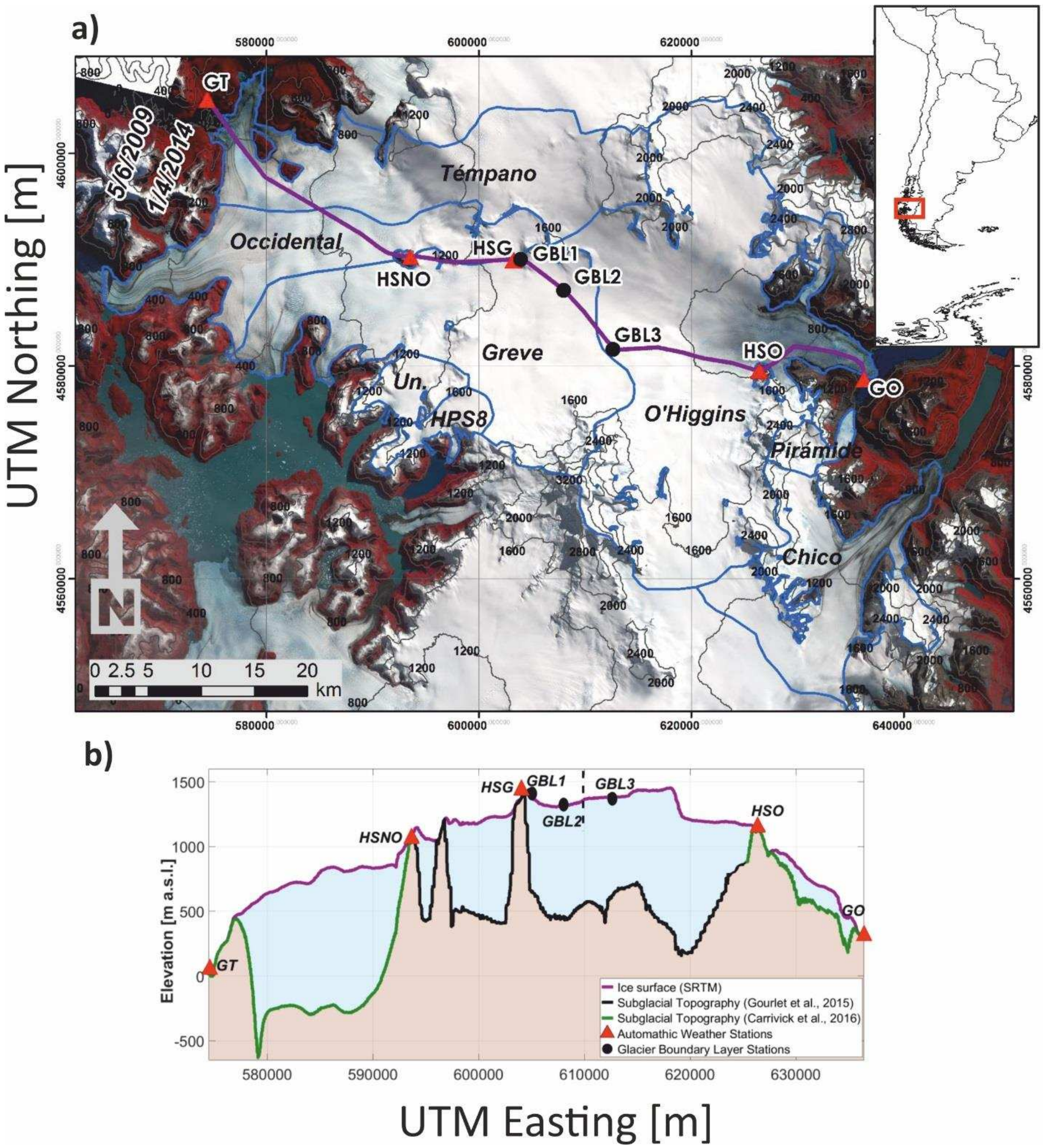
a)
b)
UTM Northing [m]
UTM Easting [m]
GT
HSNO
HSG
GBL1
GBL2
GBL3
HSO
GO
5/6/2009
1/4/2014
Témpano
Occidental
Greve
Un.
HPS8
O'Higgins
Piramide
Chico
0 2.5 5 10 15 20
km
N
Elevation [m a.s.l.]
Ice surface (SRTM)
Subglacial Topography (Gourlet et al., 2015)
Subglacial Topography (Carrivick et al., 2016)
Automathic Weather Stations
Glacier Boundary Layer Stations

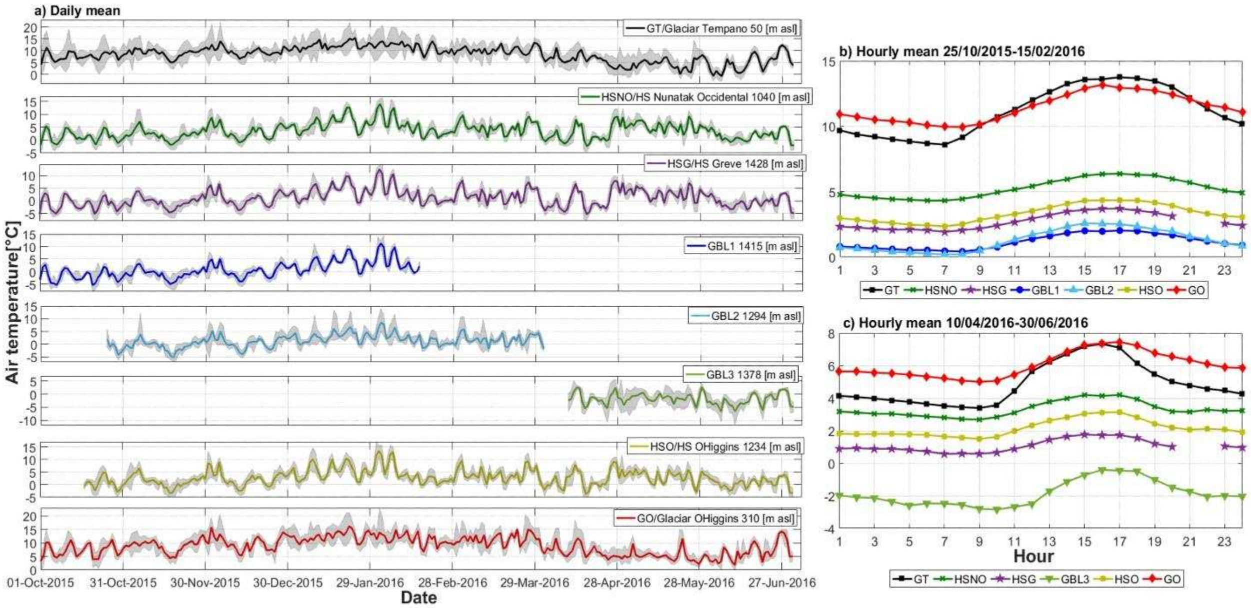
a) Daily mean
GT/Glaciar Tempano 50 [m asl]
HSNO/HS Nunatak Occidental 1040 [m asl]
HSG/HS Greve 1428 [m asl]
GBL1 1415 [m asl]
GBL2 1294 [m asl]
GBL3 1378 [m asl]
HSO/HS OHiggins 1234 [m asl]
GO/Glaciar OHiggins 310 [m asl]
Air temperature[°C]
Date
01-Oct-2015 31-Oct-2015 30-Nov-2015 30-Dec-2015 29-Jan-2016 28-Feb-2016 29-Mar-2016 28-Apr-2016 28-May-2016 27-Jun-2016
b) Hourly mean 25/10/2015-15/02/2016
GT HSNO HSG GBL1 GBL2 HSO GO
c) Hourly mean 10/04/2016-30/06/2016
Hour
GT HSNO HSG GBL3 HSO GO

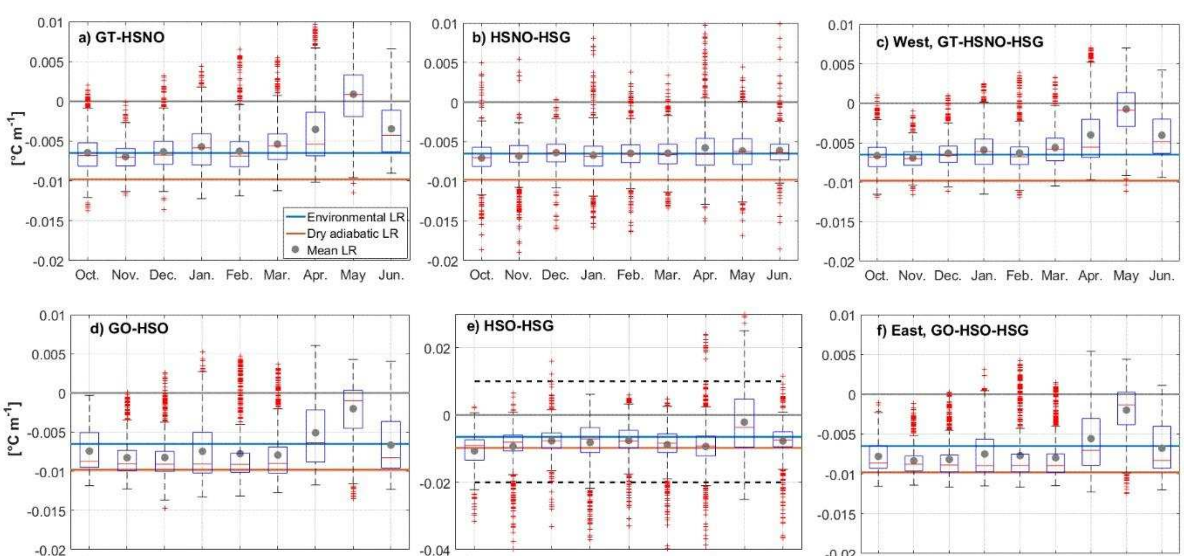
a) GT-HSNO
b) HSNO-HSG
c) West, GT-HSNO-HSG
d) GO-HSO
e) HSO-HSG
f) East, GO-HSO-HSG
[°C m^{-1}]
Environmental LR
Dry adiabatic LR
Mean LR
Oct. Nov. Dec. Jan. Feb. Mar. Apr. May Jun.

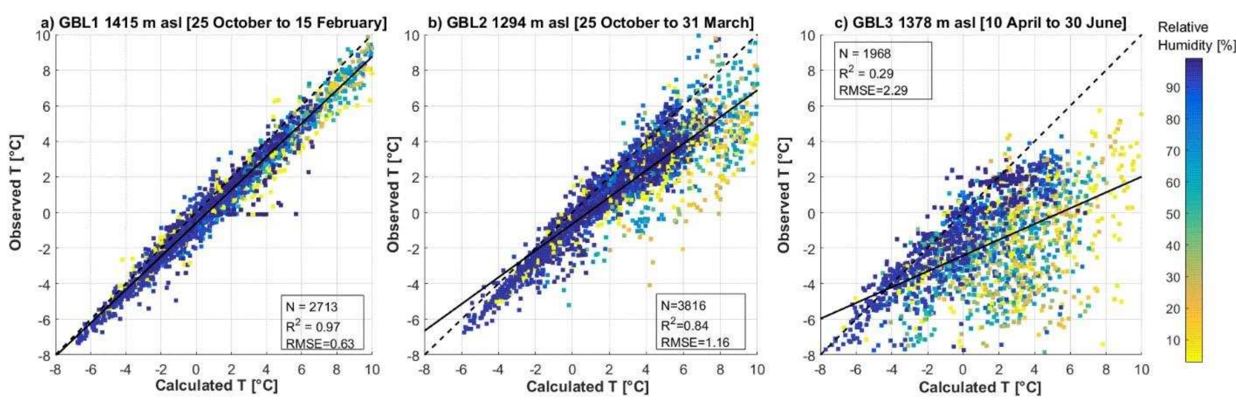
a) GBL1 1415 m asl [25 October to 15 February]
N = 2713
R² = 0.97
RMSE=0.63
b) GBL2 1294 m asl [25 October to 31 March]
N=3816
R²=0.84
RMSE=1.16
c) GBL3 1378 m asl [10 April to 30 June]
N = 1968
R² = 0.29
RMSE=2.29
Observed T [°C]
Calculated T [°C]
Relative Humidity [%]

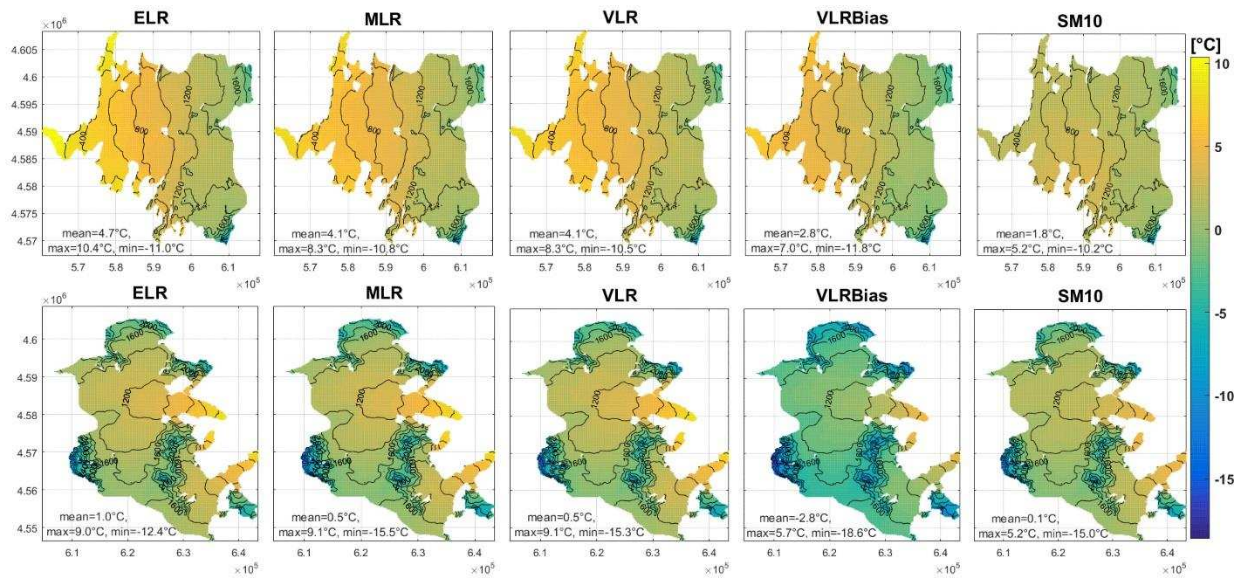
ELR
MLR
VLR
VLRBias
SM10
[°C]
mean=4.7°C, max=10.4°C, min=-11.0°C
mean=4.1°C, max=8.3°C, min=-10.8°C
mean=4.1°C, max=8.3°C, min=-10.5°C
mean=2.8°C, max=7.0°C, min=-11.8°C
mean=1.8°C, max=5.2°C, min=-10.2°C
mean=1.0°C, max=9.0°C, min=-12.4°C
mean=0.5°C, max=9.1°C, min=-15.5°C
mean=0.5°C, max=9.1°C, min=-15.3°C
mean=-2.8°C, max=5.7°C, min=-18.6°C
mean=0.1°C, max=5.2°C, min=-15.0°C

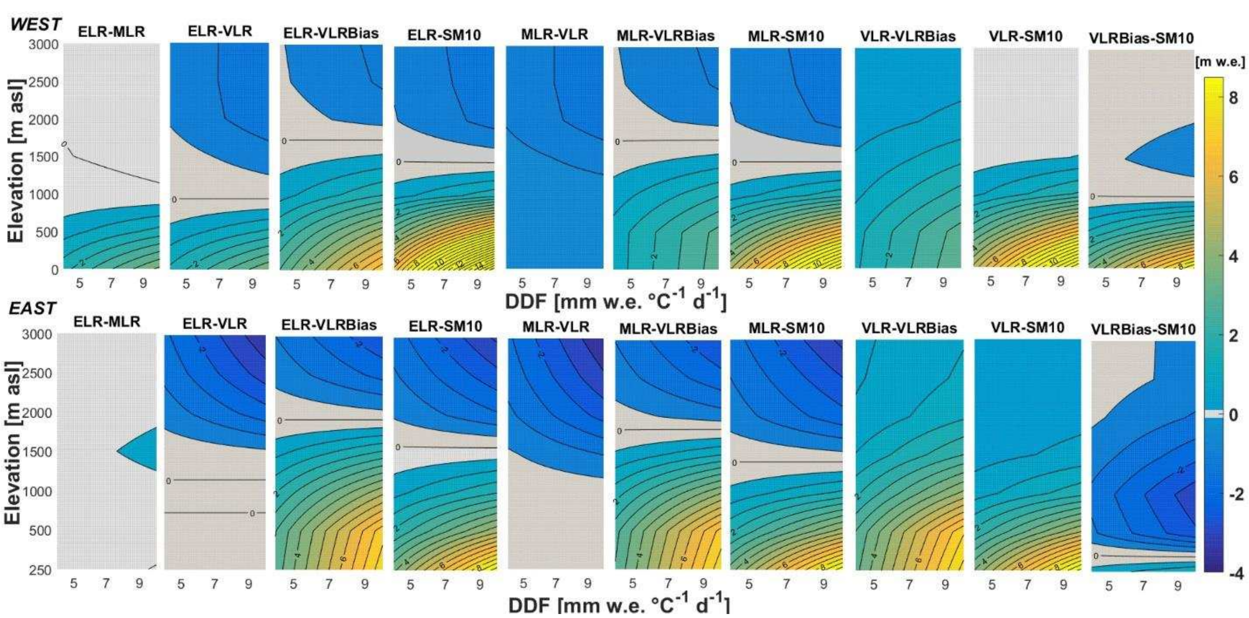
WEST
EAST
ELR-MLR
ELR-VLR
ELR-VLRBias
ELR-SM10
MLR-VLR
MLR-VLRBias
MLR-SM10
VLR-VLRBias
VLR-SM10
VLRBias-SM10
Elevation [m asl]
DDF [mm w.e. °C⁻¹ d⁻¹]
[m w.e.]

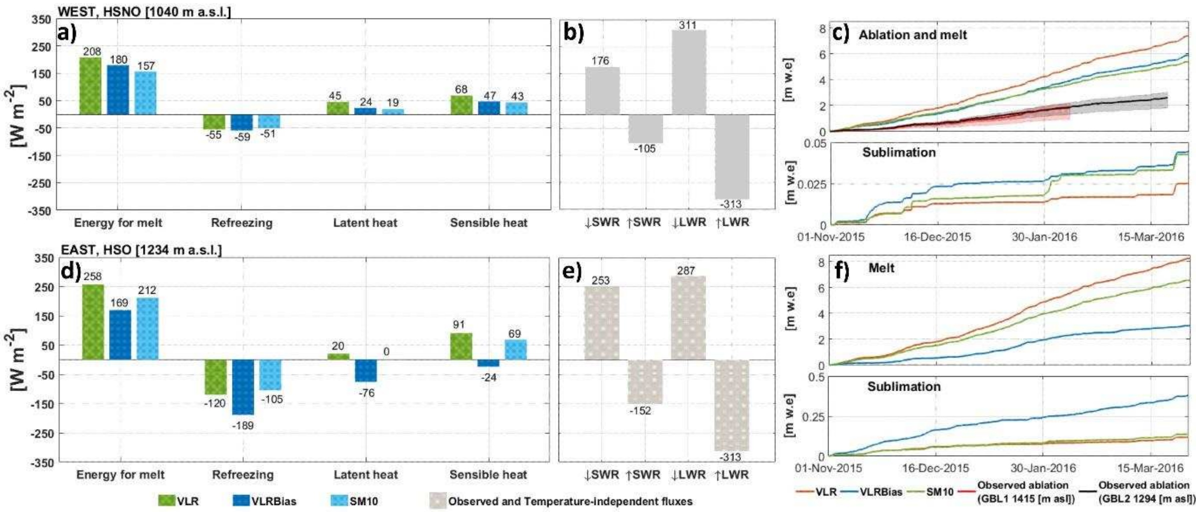
WEST, HSNO [1040 m a.s.l.]
a)
b)
c) Ablation and melt
Sublimation
EAST, HSO [1234 m a.s.l.]
d)
e)
f) Melt
Sublimation
[W m-2]
[m w.e]
Energy for melt
Refreezing
Latent heat
Sensible heat
↓SWR ↑SWR ↓LWR ↑LWR
01-Nov-2015
16-Dec-2015
30-Jan-2016
15-Mar-2016
VLR
VLRBias
SM10
Observed and Temperature-independent fluxes
Observed ablation (GBL1 1415 [m asl])
Observed ablation (GBL2 1294 [m asl])